Supplementary Information for

Millennial variability in intermediate ocean circulation and Indian monsoonal weathering inputs during the last deglaciation and Holocene

Zhaojie Yu[1, 2, 3]*, Christophe Colin[4], David J. Wilson[5], Germain Bayon[6], Zehua Song[1], Sophie Sepulcre[4], Arnaud Dapoigny[7], Yuanlong Li[8], Shiming Wan[1, 2, 3]

[1] Key Laboratory of Marine Geology and Environment, Institute of Oceanology, Chinese Academy of Sciences, Qingdao 266071, China.

[2] Laboratory for Marine Geology, Qingdao National Laboratory for Marine Science and Technology, Qingdao 266061, China.

[3] Center for Ocean Mega-Science, Chinese Academy of Sciences, Qingdao 266071, China.

[4] Université Paris-Saclay, CNRS, GEOPS, 91405, Orsay, France.

[5] Institute of Earth and Planetary Sciences, University College London and Birkbeck, University of London, Gower Street, London, WC1E 6BT, UK.

[6] IFREMER, Marine Geoscience Unit, F-29280 Plouzané, France.

[7] LSCE/IPSL, CEA-CNRS-UVSQ, Université Paris-Saclay, F-91191 Gif-sur-Yvette, France.

[8] Key Laboratory of Ocean Circulation and Waves, Institute of Oceanology, Chinese Academy of Sciences, Qingdao 266071, China

*Corresponding author:

Zhaojie Yu
Email: yuzhaojie@qdio.ac.cn.

This PDF file includes:

- Materials and methods
- Supplementary text S1 to S2
- Figures S1 to S9
- Tables S1 to S3
- SI References

Materials and methods

Core samples and age model

Core MD77-191 (7°30′ N, 76°43′ E, 1354 m, Fig. 1) was collected in the northern Indian Ocean, approximately 100 km from the south coast of India. The sediment comprises mainly terrigenous clay that is rich in foraminifera and nannofossil ooze. Its age model was established using oxygen isotope stratigraphy based on planktic foraminifera *Globigerinoides ruber*, endobenthic foraminifera *Uvigerina peregrina*, and 13 accelerator mass spectrometry (AMS) ^{14}C dates [*Bassinot et al.*, 2011; *Ma et al.*, 2020] (SFig. 3). The Bacon software, with the latest calibration curve of MARINE20, was used to convert ^{14}C ages into calendar ages [*Blaauw and Christen*, 2011; *Heaton et al.*, 2020], including a correction for the ocean surface reservoir age of -106±20 yr based on the average of 3 modern measurements near to the location of core MD77-191 [*Broecker and Peng*, 1982]. Overall, core MD77-191 provides a continuous record over the last 17 kyr, with an average sedimentation rate of approximately 25 cm/kyr and a sedimentation rate of up to 40 cm/kyr during the Holocene.

Neodymium isotope measurements on planktic foraminifera

Neodymium (Nd) isotopes were measured on 25 to 30 mg of mixed planktic foraminifera from the washed >150 μm size fraction of the samples. No oxidative-reductive leaching procedure was employed and this approach has been demonstrated to be suitable for extracting bottom water Nd isotopic compositions [*Tachikawa et al.*, 2014; *Wu et al.*, 2015]. The cleaning procedure and purification of Nd were carried out in a class 100 clean laboratory using ultrapure reagents. The foraminifera shells were crushed between two glass slides to open chambers, and the calcite fragments were ultrasonicated for 1 min in MilliQ water before pipetting off the suspended particles. This step was repeated until the water was clear and free of clay particles. Samples were inspected under a binocular microscope to ensure that all sediment particles had been removed, before they underwent a weak acid leaching for 5 min in 1 ml 0.001 M HNO_3 with ultrasonication. After the cleaning step, samples were transferred into a 1.5 ml tube, soaked in 0.5 ml MilliQ water, and dissolved using stepwise addition of 100 µl 0.5 M HNO_3 until the dissolution reaction stopped. The dissolved samples were centrifuged, and the supernatant was immediately transferred to Teflon beakers to prevent the leaching of any possible remaining phases. The solutions were then dried and Nd was purified using Eichrom TRU-Spec and Ln-Spec resins [*Wu et al.*, 2015].

The $^{143}Nd/^{144}Nd$ ratios were analysed using a Thermo Fisher Neptune Plus multi-collector inductively coupled plasma mass spectrometer (MC-ICPMS) at the LSCE in Gif-sur-Yvette, France (Table S1; SFig. 3). Sample and standard concentrations were matched at 10 to 15 ppb, and mass fractionation was corrected by normalising $^{146}Nd/^{144}Nd$ ratios to 0.7219, applying an exponential law. Samples were analyzed during 2 sessions and every two samples were bracketed with analyses of JNdi-1 Nd standard solution, which is characterised by certified values of 0.512115 ± 0.000006 [*Tanaka et al.*, 2000]. The external reproducibility (2σ), defined as 2 standard deviations of repeated measurements of the JNdi-1 standard, was between 0.24 and 0.40 ε_{Nd} units for the different analytical sessions. The analytical error reported for each sample analysis is based on the external reproducibility of the JNdi-1 standard within a given session, unless the internal error was higher. In addition, a few analyses of La Jolla standard solution were made within each session, at concentrations similar to those of the samples (i.e. 10-15 ppb), and gave values from 0.511848 ± 0.000008 to 0.511858 ± 0.000005 (2σ) after bracketing with the JNdi-1 Nd standard solution. The offset between these results and the certified value for La Jolla (0.511858 ± 0.000007) [*Lugmair and Carlson*, 1978] was less than 0.2 ε_{Nd} units for all the La Jolla analyses in this study, which supports our bracketing procedure. The Nd isotopic composition is expressed as ε_{Nd} = $[(^{143}Nd/^{144}Nd)_{Sample}/(^{143}Nd/^{144}Nd)_{CHUR} - 1] \times 10{,}000$, where $(^{143}Nd/^{144}Nd)_{CHUR} = 0.512638$ represents the chondritic uniform reservoir [*Jacobsen and Wasserburg*, 1980].

Neodymium isotopes measured on planktic foraminifera have been widely applied to trace past intermediate and deep ocean circulation [*Hu et al.*, 2016; *Piotrowski et al.*, 2012; *N L Roberts et al.*, 2010; *Tachikawa et al.*, 2014]. Most of the rare earth elements in the foraminifera are from the authigenic Fe-Mn fraction, with relatively little contained in the primary foraminiferal calcite lattice [*Palmer*, 1985; *N Roberts et al.*, 2012; *Tachikawa et al.*, 2013]. A range of analytical techniques, including NanoSIMS, electron probe microanalysis (EPMA), and scanning electron microscopy (SEM), have confirmed the significant role of Fe–Mn oxides and Mn-rich carbonates as the main Nd carrier phases in foraminifera *[Tachikawa et al., 2013]*. This situation is also supported by the studies of *Kraft et al.* [2013] and *Wu et al.* [2015], which showed that the Nd extracted from different species of planktic foraminifera, using different cleaning methods, records similar Nd isotope compositions that correspond to local bottom water signatures. It has also been demonstrated that the above conclusion applies to the Bay of Bengal *[Yu et al., 2018]*, through an assessment of Nd isotope records considering vertical seawater Nd isotope gradients from different seasons [*Singh et al.*, 2012; *Yu et al.*, 2017], cleaned foraminifera data [*Stoll et al.*, 2007], and core-top detrital sediment compositions [*Colin et al.*, 2006]. A wide range of independent studies therefore support that both cleaned and uncleaned planktic foraminifera systematically record the Nd isotope composition of bottom water or pore water.

Strontium and neodymium isotope measurements on detrital sediments

In order to assess sediment provenance in core MD77-191 over the last 17 kyr, we analyzed strontium (Sr) and Nd isotopes on the clay size fraction (<2 μm) of 17 detrital sediment samples (Table S2; SFig. 3). The sediment samples were first decarbonated using acetic acid (25 %) and organic matter was removed using hydrogen peroxide (15 %), before the <2 μm component was separated following Stokes' law. Both Sr and Nd isotopic compositions were determined on a Thermo Fisher Triton Plus TIMS at Tianjing Center, China Geological Survey, following an established method [*W G Liu et al.*, 2020]. Briefly, 100 mg of sediment powder was digested in Savillex beakers on a hotplate at 150 °C for a week, using a mixture of concentrated acids (2.5 ml HF, 0.5 ml HNO_3, and 0.015 ml $HClO_4$). Cation resin AG50W-12 and resin P507 were used to separate Sr and Nd fractions [*Yu et al.*, 2019]. Mass fractionation was corrected by normalizing to $^{88}Sr/^{86}Sr$ = 8.375209 and $^{146}Nd/^{144}Nd$ = 0.7219 for Sr and Nd, respectively. Standard solutions SRM987 and JNdi-1 were analyzed to monitor instrument performance and gave values of $^{87}Sr/^{86}Sr = 0.710242 \pm 0.000006$ (2σ) and $^{143}Nd/^{144}Nd = 0.512116 \pm 0.000007$ (2σ), respectively. International rock standard BCR-2 was analyzed to monitor the separation process, giving values of $^{87}Sr/^{86}Sr = 0.705011 \pm 0.000008$ (2σ) and $^{143}Nd/^{144}Nd = 0.512635 \pm 0.000005$ (2σ), in good agreement with published values [*Weis et al.*, 2006]. For samples, reported uncertainties (2σ) represent the external reproducibility (based on the BCR-2 rock standard) unless the internal error was higher.

Supplementary Information Text

S1. Integrated Indian Summer Monsoon (ISM) proxy

Stalagmite $\delta^{18}O$ records from the ISM-dominated region provide a robust proxy for changes in ISM rainfall, although the extent to which they quantitatively reflect precipitation amount remains debated [*Battisti et al.*, 2014; *X Liu et al.*, 2020]. To date, no continuous stalagmite $\delta^{18}O$ record spanning the last deglaciation and Holocene is available from the ISM region. We therefore extended an existing integrated ISM proxy based on multiple stalagmite records for the Holocene [*X Liu et al.*, 2020] to establish a continuous ISM proxy record for the last 17 kyr. Based on a review of South Asian stalagmites [*Kaushal et al.*, 2018], we extracted stalagmite $\delta^{18}O$ data from a total of 14 caves spanning 0-35°N, 70-95°E from the SISAL database (SFig. 4). The latest version of the database, SISAL_v2.0, is available at http://dx.doi.org/10.17864/1947.256 [*Comas-Bru et al.*, 2020]. To produce the integrated record, these stalagmite data were first linearly interpolated to a 50-year resolution. Such interpolation of the data series does not change the original patterns in the data. Each data set was then normalised to an interval of [0-1] using the following equation:

$$x_n = \frac{x_i - x_{min}}{x_{max} - x_{min}}$$

where x_n is the preliminary normalised value, x_i is the interpolated stalagmite isotope value, x_{max} and x_{min} are the maximum and minimum values of the interpolated stalagmite data. Finally, values from different data sets in the same time period were averaged [*X Liu et al.*, 2020]. Note that because lower stalagmite $\delta^{18}O$ values represent higher ISM rainfall, we use the equation:

$$y = 1 - x_n$$

where y is an integrated index of ISM precipitation, in order that high normalised values represent high precipitation (SFig. 5).

The integrated ISM proxy displays a long-term evolution that mirrors summer (June) isolation at 30°N [*Laskar et al.*, 2004], but also contains significant millennial-scale variability, with weakening clearly expressed during Heinrich Stadial 1 (HS1) and the Younger Dryas (YD) (Fig. 2, SFig. 6a). Similar patterns are recorded in two independent marine records from the northern Bay of Bengal: a sea surface salinity reconstruction from core SO93-126KL (correlation with integrated ISM proxy gives $R^2 = 0.58$, $p < 0.001$, $n = 338$; SFig. 4c) [*Kudrass et al.*, 2001], and an ISM rainfall proxy based on $\delta D_{alkanes}$ in core SO188-342KL ($R^2 = 0.67$, $p < 0.001$, $n = 91$; SFig. 6b) [*Contreras-Rosales et al.*, 2014]. The ISM proxy also shows a close correlation with the integrated Chinese cave stalagmite $\delta^{18}O$ reconstruction ($R^2 = 0.83$, $p < 0.001$, $n = 338$; SFig. 6d) [Cheng et al., 2016]. We note that three of the individual records (from Mawmluh, Kalakot, and Kotumsar caves) contain data in the interval from 8 - 10 ka, with only the Mawmluh cave record completely covering this interval (SFig. 4 and 5). Although limited by the amount of stalagmite $\delta^{18}O$ data available from 8 - 10 ka, the good correspondence between the integrated ISM proxy and both the Chinese cave stalagmite $\delta^{18}O$ and two independent monsoon indicators (SFig. 6) supports its utility.

We also note that stalagmite $\delta^{18}O$ values can reflect multiple processes besides the amount effect, and that records from different geographic locations will reflect different interactions between these processes and different local amount effect relationships [*Battisti et al.*, 2014; *Kaushal et al.*, 2018; *X Liu et al.*, 2020]. However, since they are qualitatively correlated, the weighted average of speleothem $\delta^{18}O$ values from different caves after [0-1] normalization seems to be a reasonable approach to obtain a continuous stalagmite record. Such a method has also been successfully used before [*X Liu et al.*, 2020]. Overall, the good agreement, on both orbital and millennial timescales, among four independent approaches (SFig. 6) supports the robustness of the integrated stalagmite-based proxy as a record of the ISM. In addition, and in contrast to the marine records, it also benefits from a precise absolute-dated age scale, so we focus on comparison to the integrated ISM record in the main text.

S2. Estimation of Antarctic Intermediate Water (AAIW) advection

In the modern day, bottom waters at core MD77-191 are dominated by modified southern-sourced waters, with only minor contributions from Persian Gulf Water and Red Sea Water that together comprise less than 15% at comparable depths of the nearby seawater station 0805 [*Goswami et al.*, 2014] (Fig. 1). Those latter water masses, which form during winter cooling in those marginal seas [*Prasad et al.*, 2001], therefore have little impact on the local dissolved Nd budget, and likely had even less influence during the time intervals of HS1, the YD, and the Early Holocene. During HS1 and the YD, significantly lower sea levels than at present would have further restricted the production and outflow of Persian Gulf Water and Red Sea Water [*Rohling and Zachariasse*, 1996]. Although Red Sea Water formation may have strengthened during the Early Holocene [*S. J. A. Jung et al.*, 2001], its transport towards the core site of MD77-191 requires southward flow along the west coast of India during the winter monsoon season [*Prasad et al.*, 2001], which would have been significantly hindered by the intensified ISM and weak winter monsoon at this time. Benthic oxygen isotope data in core MD77-191 also argue against any significant contributions from Red Sea Water during this interval [*Ma et al.*, 2020]. We therefore rule out variations in the overflows from marginal seas as a control on the foraminiferal Nd isotope record of core MD77-191, and instead focus on the potential influence of southern-sourced intermediate waters.

The foraminiferal Nd isotope record of core MD77-191 was mainly influenced by changes in two end-members: (i) changes in regional continental chemical weathering fluxes associated with precipitation changes in the river catchments; and (ii) variability in the Nd isotopic composition and flow strength of southern-sourced intermediate waters. In the modern southwest Indian Ocean, AAIW has a Nd isotopic composition of approximately −9 to −8 [*Amakawa et al.*, 2019], while shifts of ~1-2 ε_{Nd} units towards more radiogenic compositions at the Last Glacial Maximum have been observed for AAIW in other sectors of the Southern Ocean [*Hu et al.*, 2016]. Such changes presumably reflect reduced contributions of North Atlantic Deep Water to the glacial Southern Ocean [*Robinson and van de Flierdt*, 2009], as well as possibly reflecting variability in the North Atlantic Deep Water end-member [*Du et al.*, 2020; *Zhao et al.*, 2019]. If similarly modest deglacial AAIW end-member changes also applied to AAIW in the Indian Ocean sector, then changes of AAIW flow strength, rather than its composition in its source areas, were likely the main factor that determined its contribution to Nd isotope changes in the northern Indian Ocean. Nevertheless, the effect of the AAIW end-member changes can be incorporated, allowing the effect of AAIW advection to be estimated, by using a two end-member mixing model with the following mixing equations:

$$[Nd]_A = [Nd]_w * f_w + [Nd]_s * (1 - f_w)$$

$$(\varepsilon_{Nd})_A = \frac{(\varepsilon_{Nd})_w * [Nd]_w * f_w + (\varepsilon_{Nd})_s * [Nd]_s * (1 - f_w)}{[Nd]_w * f_w + [Nd]_s * (1 - f_w)}$$

where f, [Nd] and ε_{Nd} are the contribution coefficient, Nd concentration and Nd isotopic composition, and w, s, and A represent the end-members of weathering inputs, AAIW, and foraminiferal values in core MD77-191, respectively.

It is challenging to obtain continuous records of past changes in Nd isotopes from the intermediate-depth Southern Ocean, and in particular no such deglacial record exists from intermediate depths of the Indian Ocean sector of the Southern Ocean. In addition, the Nd isotopic composition of the regional weathering inputs to the northern Indian Ocean could also have changed through time. In order to assess the effect of uncertainty in the end-members, we adopt sensitivity tests for the two-end-member mixing calculation using (i) the weathering end-member: a constant ε_{Nd} value of –16 or the detrital Nd isotope record from core MD77-191; (ii) the southern-sourced water mass end-member (AAIW): ODP Site 1087 (31°27.88′S, 15°18.65′E, water depth 1372 m, SFig. 7a) or core Y9 (48°14.21′S, 177°20.67′E, water depth 1267 m, SFig. 7a) [*Hu et al.*, 2016]. A typical Southern Ocean intermediate water Nd concentration of 17 pmol/kg was used and assumed to remain constant throughout the calculation [*Pena et al.*, 2013]. The ISM proxy was used to provide an estimate of the time-varying Nd concentration of the dissolved weathering inputs by making the simplifying assumption that the effective Nd concentration of the weathering inputs reaching this region of the Indian Ocean was proportional to the riverine weathering flux inputs, and that the latter were proportional to changes in the monsoon precipitation. The difference in dissolved Nd concentration between intermediate depths of the northern Indian Ocean (31.1 pmol/kg, at a water depth of 1200 m at station 0812) [*Singh et al.*, 2012] and typical Southern Ocean intermediate water (Nd concentration of 17 pmol/kg) was used to establish a coefficient between the integrated ISM proxy value from closest to the present day (i.e. 0.52 at 0.5 ka) and the Nd input flux. By multiplying the past integrated ISM values by this coefficient, we reconstructed variability in the Nd flux of past weathering inputs. Therefore, based on the known ε_{Nd} values and [Nd] of both end-members and the measured foraminiferal ε_{Nd} in core MD77-191, we estimated the southern-sourced water mass (AAIW) contributions for the last 17 kyr. For this calculation, all data were interpolated to the same time interval of 0.2 kyr.

From the comparison of panels (a) to (b) and/or (c) to (d) in SFig. 8, we can see that using ODP Site 1087 or core Y9 only leads to minor differences in the absolute value of the AAIW contribution, while there is little change in the trend. This insensitivity arises because the general trends of seawater ε_{Nd} values from ODP Site 1087 and core Y9 are similar, with only modest differences in absolute values, which are more radiogenic in core Y9 (SFig. 7a).

From the comparison of panels (b) to (c) and/or (a) to (d) in SFig. 8, where the weathering end-member is either constant (ε_{Nd} = –16) or matches the detrital Nd isotope record from core MD77-191 (which varies over time), we also observe similar trends in the calculated contribution of AAIW through time. Differences arise mainly during the deglaciation, with the results using the core MD77-191 detrital sediment record showing a relatively lower contribution from AAIW (SFig. 8a,b), due to two radiogenic ε_{Nd} values exhibited by the detrital record during the deglaciation at 12.2 and 15.0 ka (Fig. 2). Although limited by some uncertainty due to the lower resolution of the detrital record compared to the foraminiferal record, we consider the varying detrital record from core MD77-191 may provide a more reliable estimate of the composition of regional weathering inputs compared to the assumption of a constant ε_{Nd} value of –16. Therefore, we only show the calculations using the detrital record from MD77-191 as the weathering ε_{Nd} end-member (SFig. 8a,b) in the main text.

We recognise that the relationship between the integrated ISM proxy and the weathering flux of dissolved Nd is unlikely to be perfectly linear, that a detrital Nd isotope record may not perfectly represent those inputs, and that the estimate of AAIW contributions is also sensitive to the resolution and accuracy of the record used to represent the AAIW end-member. However, these approaches are considered to represent a reasonable first-order approximation for our record. Therefore, we interpret the calculated AAIW fraction as an indicator of relative (rather than absolute) changes in AAIW contributions through time. Note also that we are not able to distinguish between Upper Circumpolar Deep Water and AAIW inflows on the basis of Nd isotopes, and therefore use AAIW as a general term to refer to all intermediate waters sourced from the Southern Ocean.

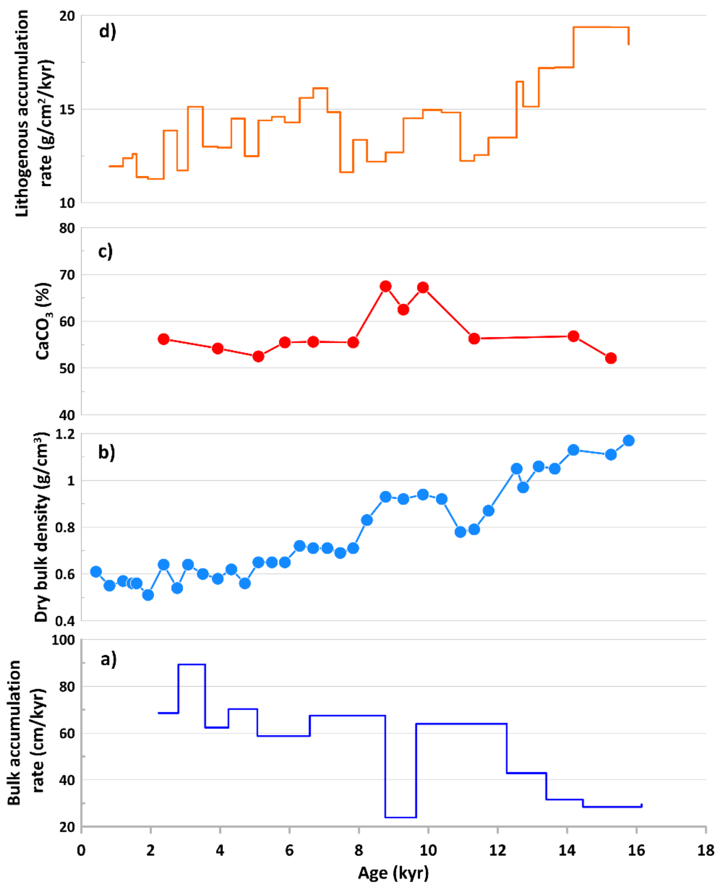

SFig. 1 Sedimentology parameters in core MD77-191. (a) Bulk accumulation rate; (b) Dry bulk density; (c) $CaCO_3$%; (d) lithogenous accumulation rate calculated using bulk accumulation rate, dry bulk density and $CaCO_3$%, assuming a negligible organic matter content. The $CaCO_3$% was interpolated to the same resolution as the bulk accumulation rate and dry bulk density. Core MD77-191 has a generally increasing bulk accumulation rate and a roughly linear increasing dry bulk density due to compaction effects. The $CaCO_3$ content is generally between 50% and 60%, with the exception of higher values reaching closer to 70% during the early Holocene from ~11-9 ka. We don't have an organic content data for this core, however, the organic content is generally lower than 5%, as shown in other cores from this region [*Colin et al.*, 1999; *Yu et al.*, 2020]. The calculated detrital accumulation rates were generally stable with ranges between 10 to 15 g/cm^2/kyr during the Holocene, and relative higher values between 15-20 g/cm^2/kyr during the last deglacial. Data source: https://doi.pangaea.de/10.1594/PANGAEA.77650.

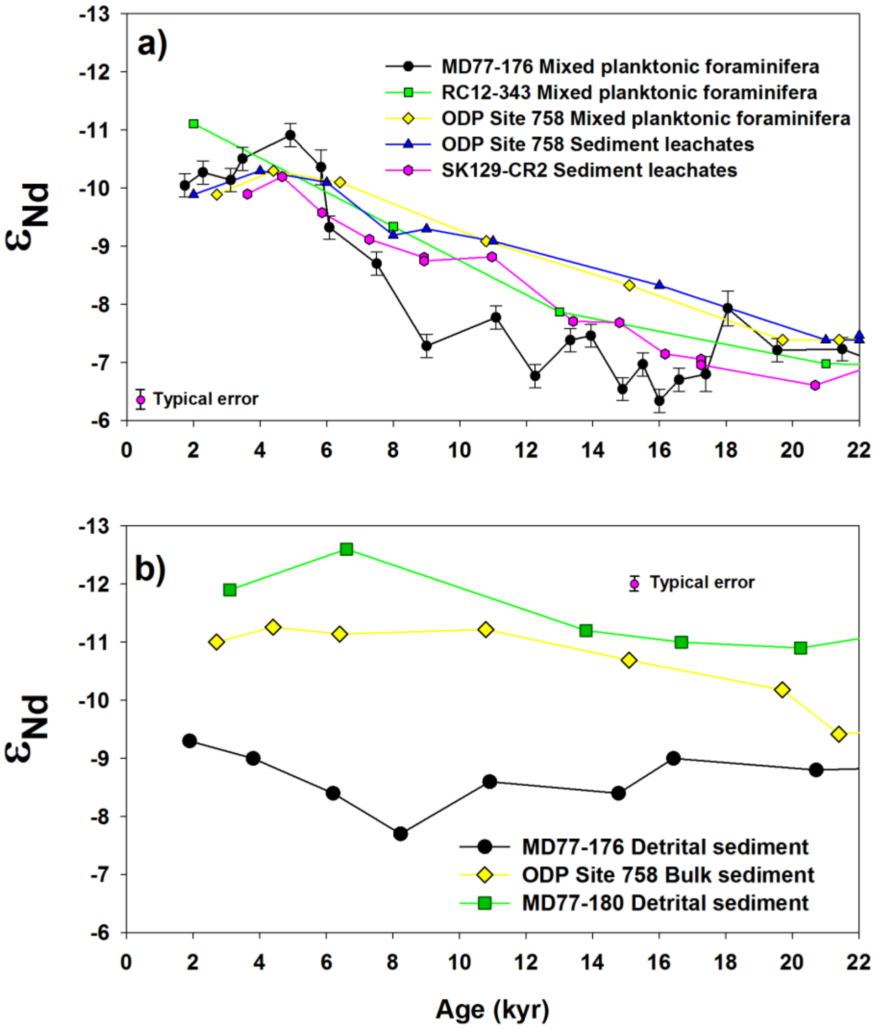

SFig. 2 Comparison of (a) Nd isotopes of foraminifera and sediment leachates, and (b) Nd isotopes of sediment in the Northern Indian Ocean. Reference: MD77-176 [*Colin et al.*, 2006; *Yu et al.*, 2018]; ODP 758 [*Burton and Vance*, 2000]; MD77-180 [*Colin et al.*, 1999] and RC12-343 [*Stoll et al.*, 2007]; SK129-CR2 [*Wilson et al.*, 2015]. The foraminiferal Nd isotope records from different cores in the Northern Indian Ocean with different lithologies have similar trends, with variations up to ~4-5 ε_{Nd} units between the LGM (22-18 ka) and mid-Holocene (6-4 ka) in each record. In contrast, the detrital Nd isotope records are generally flat, with changes of less than 2 ε_{Nd} units between the LGM (22-18 ka) and mid-Holocene (6-4 ka) in each case.

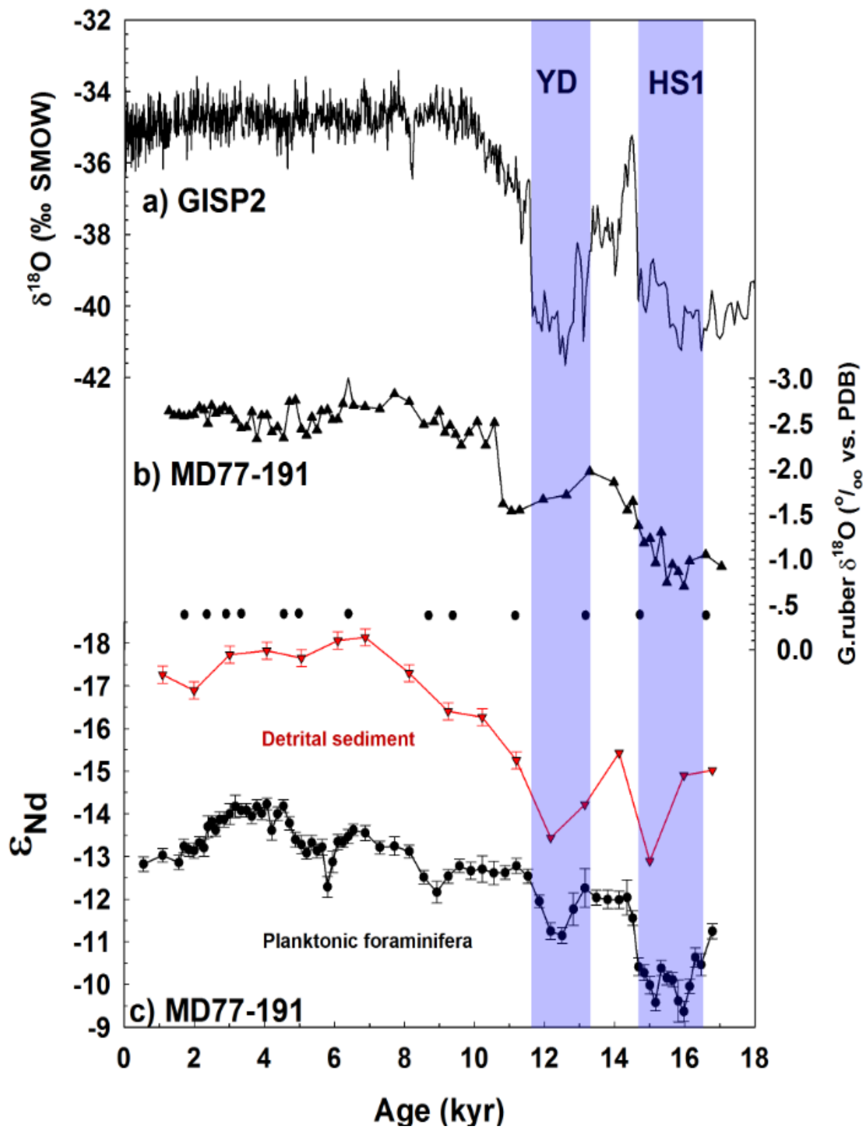

SFig. 3 Deglacial and Holocene records from core MD77-191 in the northern Indian Ocean. (a) Greenland ice core $\delta^{18}O$ record from GISP2 [*Grootes and Stuiver*, 1997]. (b) Planktic foraminiferal $\delta^{18}O$ from *G. ruber* in core MD77-191 [*Ma et al.*, 2020]. The black circles represent calibrated ^{14}C ages. (c) Nd isotope records from the clay-sized fraction of the detrital sediment (red) and from mixed planktic foraminifera (black) in core MD77-191 (this study). Vertical blue bars indicate the approximate timing of Heinrich Stadial 1 (HS1) and the Younger Dryas (YD). Error bars on Nd isotope records are 2σ.

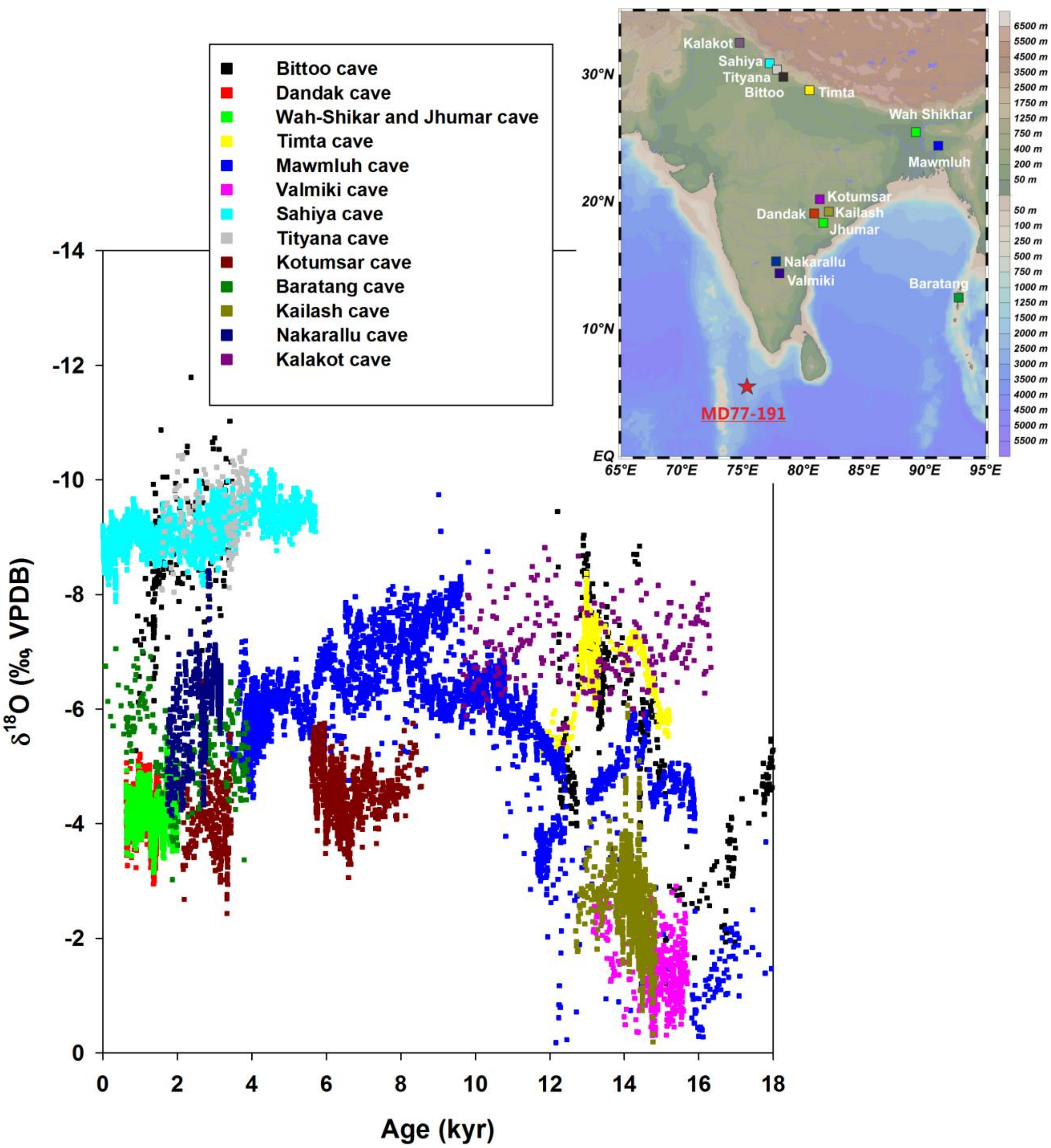

SFig. 4 Comparison of stalagmite $\delta^{18}O$ records from the ISM-dominated region, extracted from the SISAL database [*Comas-Bru et al.*, 2020; *Kaushal et al.*, 2018]. The position and names of the caves are marked in the topographic map in the upper right, with symbol colours matching the plotted data points, and the location of core MD77-191 is shown with a red star.

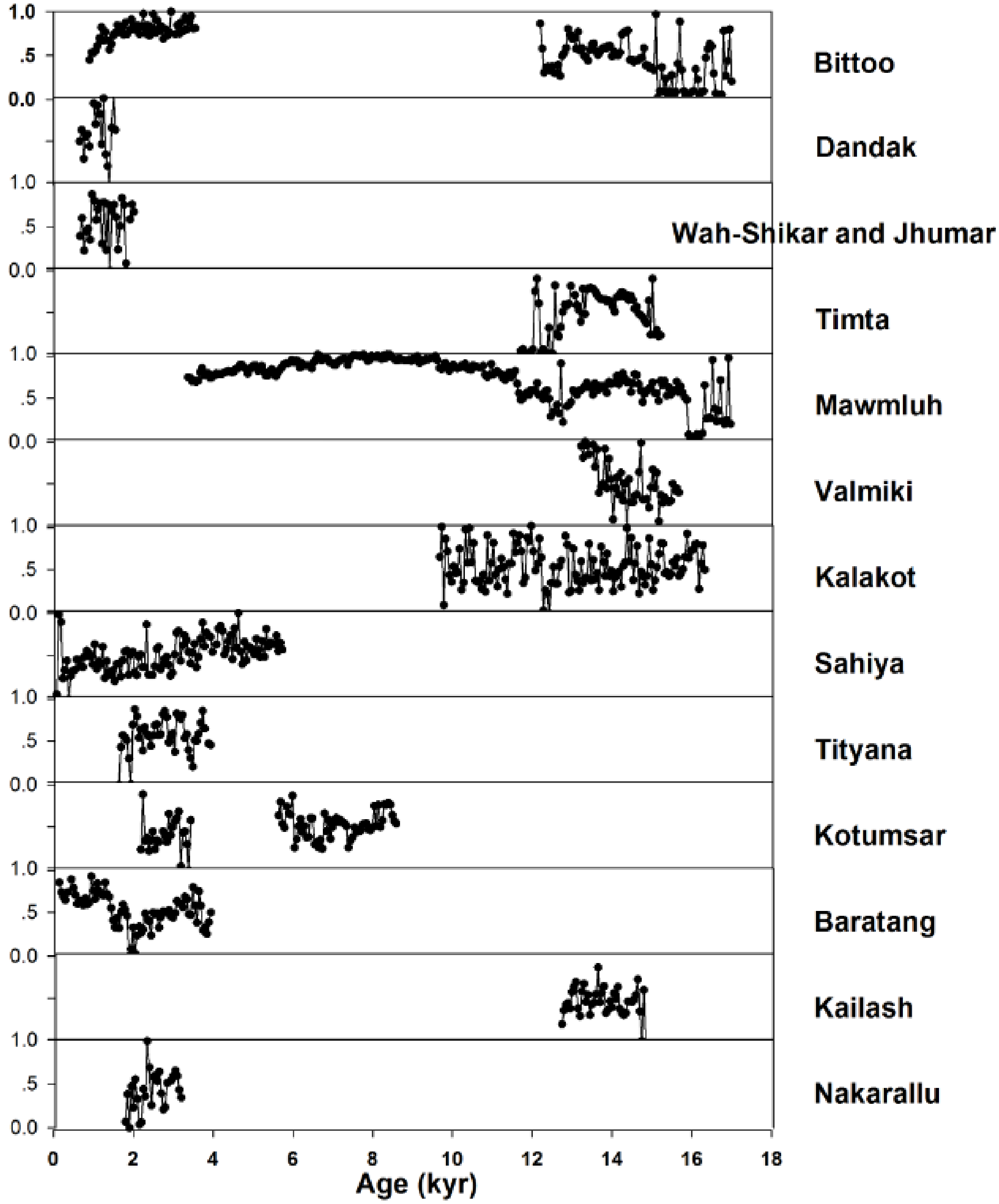

SFig. 5 Comparison of stalagmite $\delta^{18}O$ records from the ISM-dominated region (SFig. 4) after normalisation to an interval of [0-1], and plotted with higher values indicating higher precipitation. The names of the caves are marked on the right.

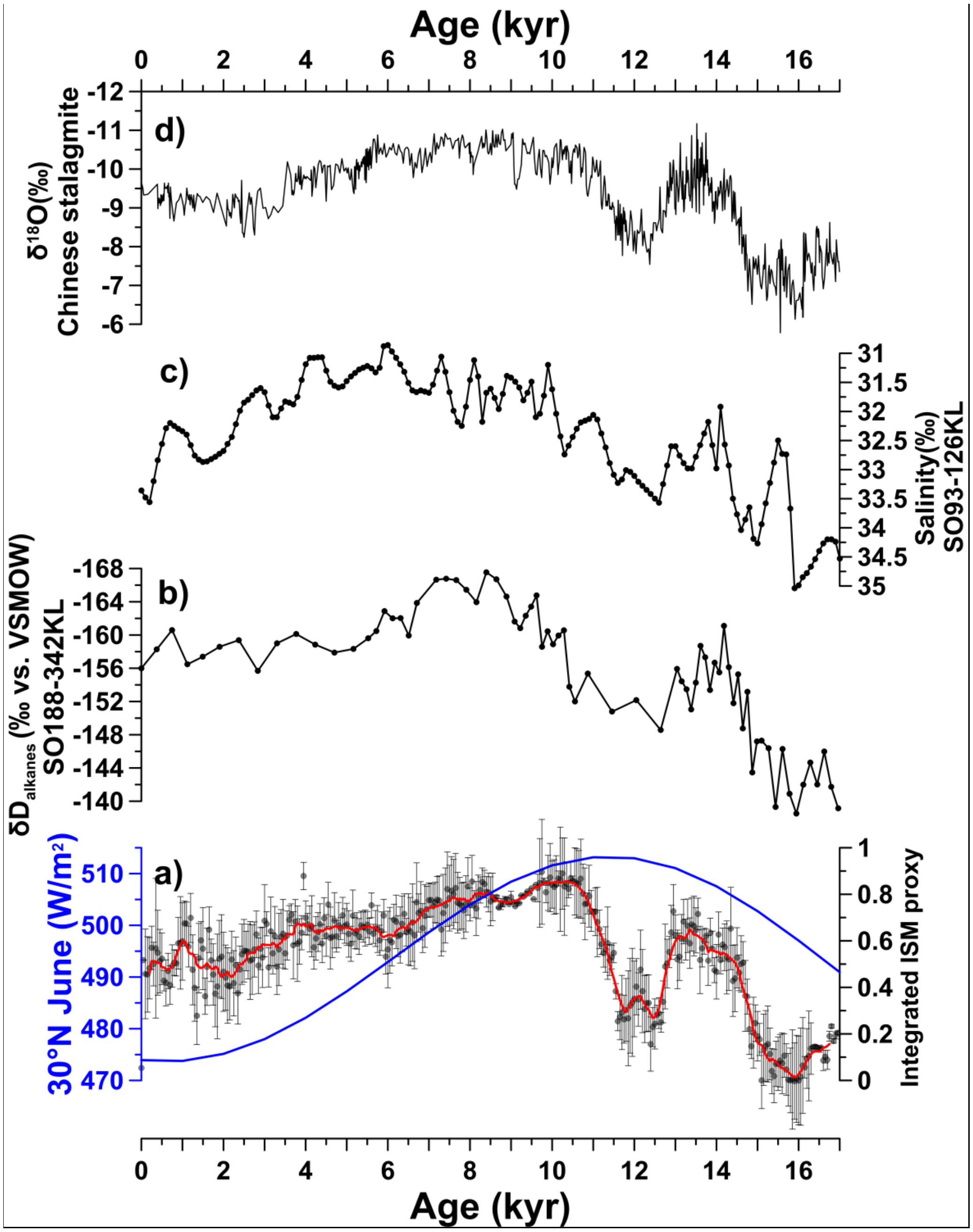

SFig. 6 Comparison of ISM proxies. (a) Integrated ISM proxy from stalagmite $\delta^{18}O$ records (grey points, with a temporally varying error calculated using the double standard deviation of the overlapped intervals; red curve is a running mean with a window width of 9) and summer (June) isolation at 30°N (blue curve). (b) ISM rainfall proxy based on $\delta D_{alkanes}$ in core SO188-342KL [*Contreras-Rosales et al.*, 2014]. (c) Sea surface salinity reconstruction from northern Bay of Bengal core SO93-126KL [*Kudrass et al.*, 2001]. (d) Integrated Chinese cave stalagmite $\delta^{18}O$ records *[Cheng et al., 2016]*.

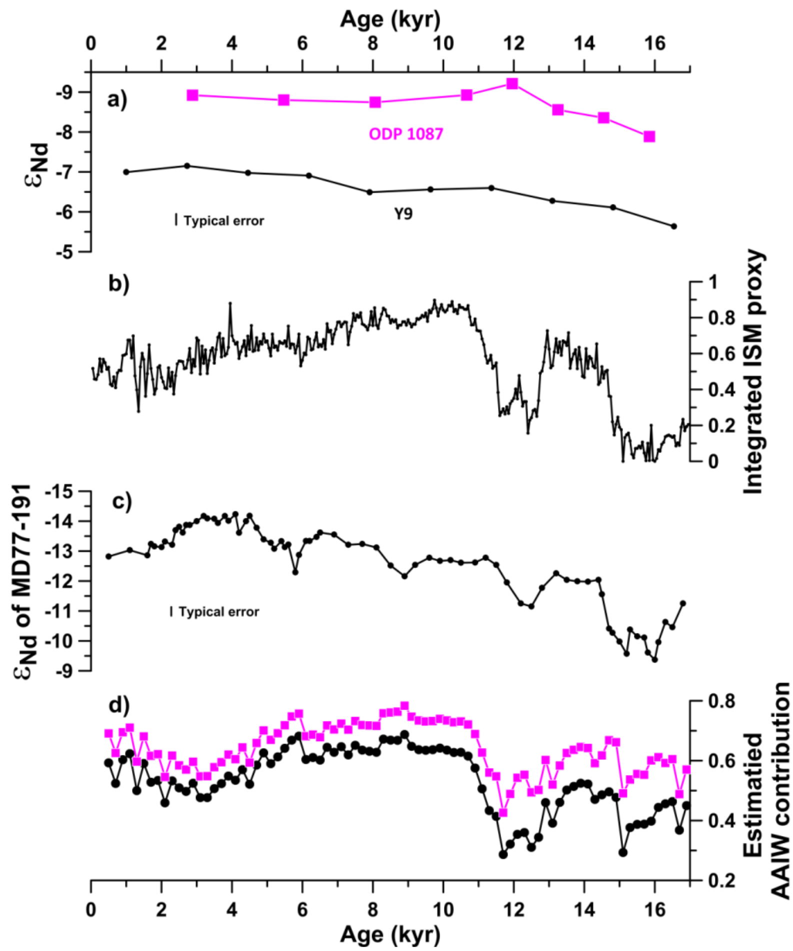

SFig. 7 Estimates of the AAIW contribution at core MD77-191, based on a mixing model in which foraminiferal ε_{Nd} values result from a mixture of AAIW advection and regional weathering inputs. (a) Seawater ε_{Nd} reconstructions from ODP Site 1087 (magenta line) and core Y9 (black line) [*Hu et al.*, 2016], used to provide estimates of the AAIW end-member. (b) Integrated ISM proxy, used to provide an estimate of the time-varying Nd flux of the dissolved inputs from regional weathering. (c) Foraminiferal ε_{Nd} values from core MD77-191. (d) Estimated AAIW contribution at core MD77-191, calculated using the Nd isotope records from ODP Site 1087 (magenta line) or core Y9 (black line) as the AAIW end-member; the detrital Nd isotope record in core MD77-191 as the weathering inputs end-member. All the curves were interpolated to the same time interval of 0.2 kyr before the calculation. Note that the calculations using two different AAIW end-members (from the Atlantic and Pacific sectors of the Southern Ocean) provide a sensitivity test, and indicate very similar changes through time, with an absolute difference of approximately 10 %

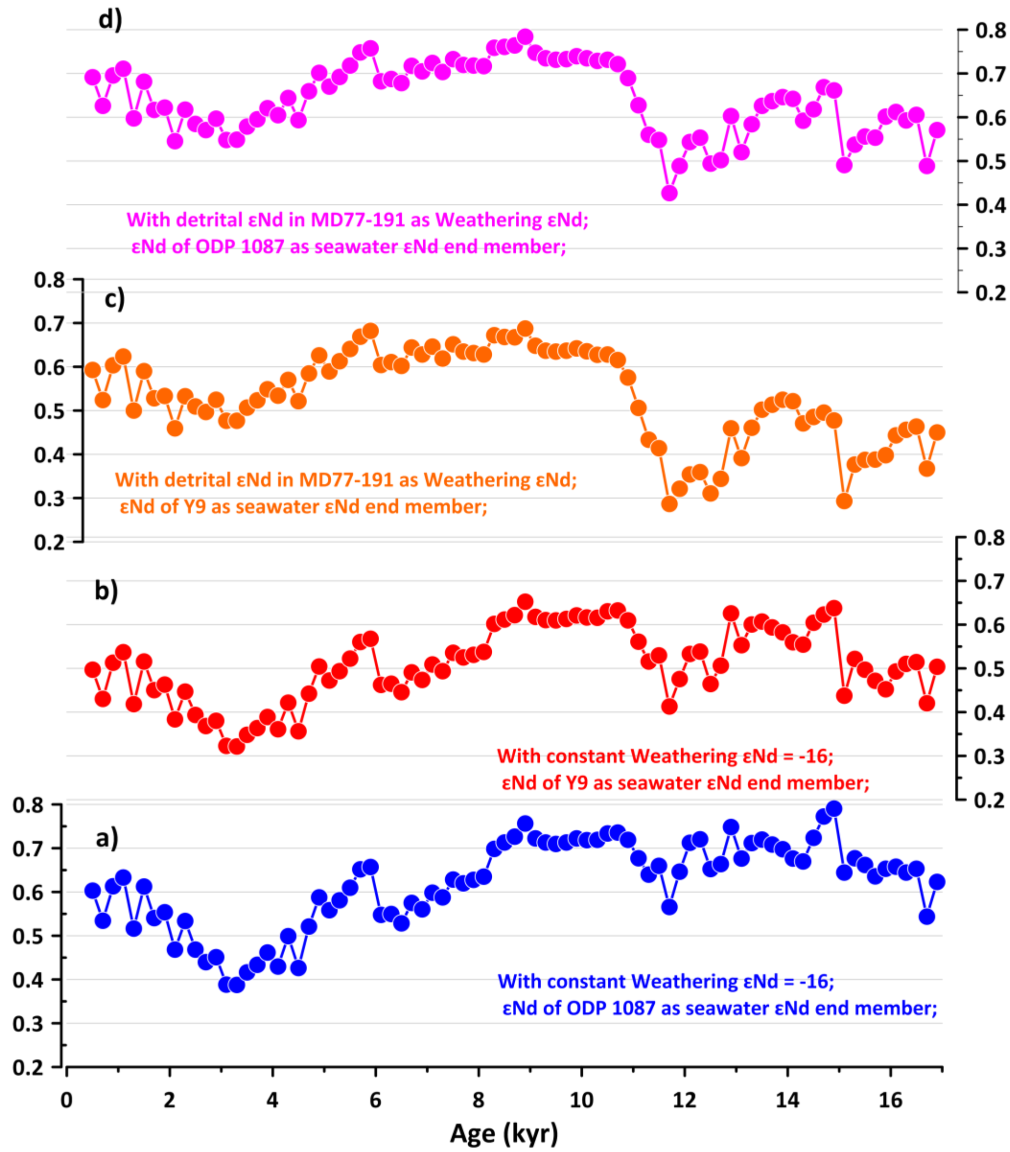

SFig. 8 Sensitivity tests for the two end-member mixing calculation varying (i) the weathering end-member: a constant ε_{Nd} value of –16 (panels a and b) or the detrital ε_{Nd} record from core MD77-191 (panels c and d); (ii) the southern-sourced water mass ε_{Nd} end-member (AAIW): ODP Site 1087 (panels a and d) or core Y9 (panels b and c). To better compare the changes, all y-axis scales (which show the contribution of southern-sourced water masses to the Nd signal) are the same.

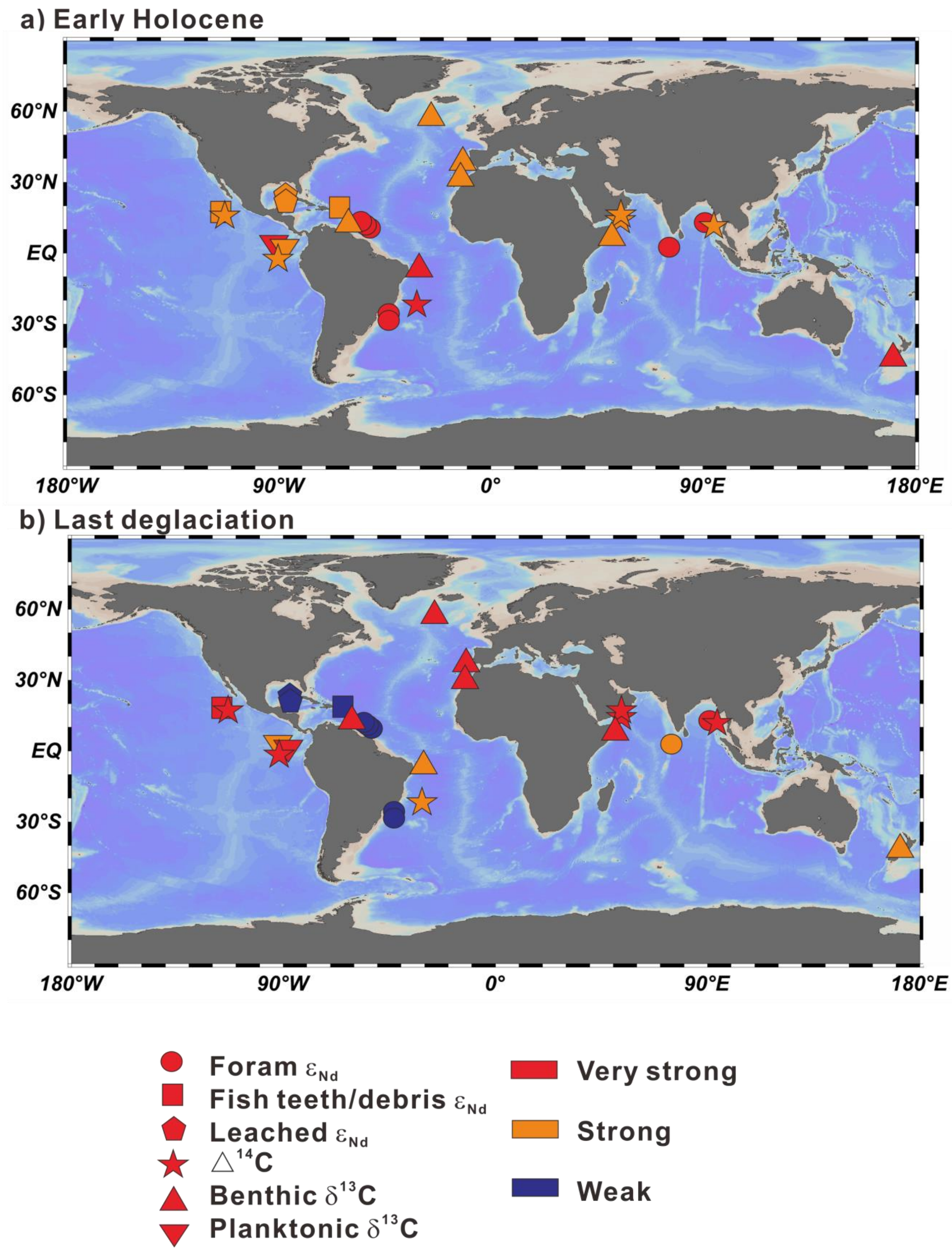

SFig. 9 Compilation of AAIW proxies indicating AAIW intensity/presence in the Indian, Pacific, and Atlantic Oceans during (a) the Early Holocene and (b) the last deglaciation. Different symbols indicate different proxies and/or archives, while different colours indicate the inferred intensity of AAIW advection. See Table S3 for core details and references.

Table S1: Nd isotope composition obtained on mixed planktic foraminifera from core MD77-191. ε_{Nd} values were calculated using a CHUR value of 0.512638 [Jacobsen and Wasserburg, 1980] as follows: ε_{Nd} =[($^{143}Nd/^{144}Nd)_{meas}$/0.512638 - 1] * 10000. The external reproducibility (2σ), defined as 2 standard deviations of repeated measurements of the JNdi-1 standard during the different measurement sessions, was between 0.24 and 0.40 ε_{Nd} units. All error bars in the text and the figures correspond to this external reproducibility, with the exception of a few samples (n=4) where the 2σ standard internal error of the individual measurements is slightly higher and has been used instead.

Depth (cm)	Age (kyr)	$^{143}Nd/^{144}Nd$	± 2 sigma	ε_{Nd}	± 2 sigma
10	0.5	0.511982	0.000012	-12.82	0.24
20	1.1	0.511971	0.000012	-13.03	0.24
30	1.6	0.511980	0.000012	-12.86	0.24
40	1.7	0.511960	0.000012	-13.24	0.24
50	1.8	0.511964	0.000012	-13.16	0.24
60	2	0.511966	0.000012	-13.13	0.24
70	2.1	0.511956	0.000012	-13.32	0.24
80	2.3	0.511962	0.000012	-13.21	0.24
90	2.4	0.511936	0.000020	-13.70	0.40
100	2.5	0.511931	0.000012	-13.81	0.24
110	2.6	0.511941	0.000012	-13.62	0.24
120	2.7	0.511928	0.000012	-13.87	0.24
130	2.8	0.511928	0.000012	-13.87	0.24
140	3	0.511921	0.000013	-14.00	0.25
150	3.2	0.511911	0.000020	-14.17	0.40
160	3.3	0.511917	0.000012	-14.09	0.24
170	3.5	0.511917	0.000012	-14.08	0.24
180	3.6	0.511924	0.000012	-13.94	0.24
190	3.8	0.511913	0.000012	-14.17	0.24
200	3.9	0.511921	0.000012	-14.01	0.24
210	4.1	0.511910	0.000012	-14.23	0.24
220	4.2	0.511940	0.000020	-13.61	0.40
230	4.4	0.511921	0.000012	-14.00	0.24
240	4.5	0.511912	0.000012	-14.18	0.24
250	4.7	0.511932	0.000012	-13.78	0.24
260	4.9	0.511952	0.000012	-13.39	0.24
270	5.1	0.511957	0.000020	-13.28	0.40

280	5.2	0.511968	0.000012	-13.08	0.24
290	5.4	0.511956	0.000012	-13.33	0.24
300	5.5	0.511966	0.000012	-13.13	0.24
310	5.6	0.511961	0.000012	-13.22	0.24
320	5.8	0.512009	0.000013	-12.29	0.25
330	5.9	0.511978	0.000020	-12.87	0.40
340	6.1	0.511955	0.000012	-13.34	0.24
350	6.2	0.511955	0.000012	-13.34	0.24
360	6.4	0.511948	0.000012	-13.47	0.24
370	6.5	0.511941	0.000012	-13.62	0.24
380	6.9	0.511944	0.000012	-13.55	0.24
390	7.3	0.511962	0.000012	-13.21	0.24
400	7.7	0.511959	0.000020	-13.24	0.40
410	8.1	0.511966	0.000012	-13.12	0.24
420	8.5	0.511997	0.000012	-12.52	0.24
430	8.9	0.512015	0.000020	-12.16	0.40
440	9.2	0.511996	0.000012	-12.54	0.24
450	9.6	0.511984	0.000012	-12.78	0.24
460	9.9	0.511990	0.000012	-12.67	0.24
470	10.2	0.511988	0.000016	-12.70	0.31
480	10.5	0.511991	0.000020	-12.61	0.40
490	10.9	0.511992	0.000012	-12.62	0.24
500	11.2	0.511984	0.000012	-12.78	0.24
510	11.5	0.511996	0.000012	-12.54	0.24
520	11.8	0.512026	0.000012	-11.95	0.24
530	12.2	0.512062	0.000012	-11.25	0.24
540	12.5	0.512068	0.000012	-11.15	0.24
550	12.8	0.512035	0.000020	-11.77	0.40
560	13.2	0.512011	0.000023	-12.26	0.45
570	13.5	0.512022	0.000012	-12.04	0.24
580	13.8	0.512024	0.000012	-11.99	0.24
590	14.1	0.512025	0.000012	-11.98	0.24
600	14.4	0.512021	0.000021	-12.04	0.41
610	14.5	0.512047	0.000012	-11.56	0.24
620	14.7	0.512105	0.000012	-10.41	0.24
630	14.8	0.512112	0.000012	-10.27	0.24
640	15	0.512127	0.000012	-9.98	0.24
650	15.2	0.512148	0.000012	-9.57	0.24

660	15.3	0.512107	0.000012	-10.38	0.24
670	15.5	0.512118	0.000012	-10.15	0.24
680	15.7	0.512121	0.000012	-10.11	0.24
690	15.8	0.512145	0.000025	-9.61	0.49
700	16	0.512159	0.000012	-9.37	0.24
710	16.1	0.512129	0.000012	-9.96	0.24
720	16.3	0.512094	0.000012	-10.63	0.24
730	16.5	0.512103	0.000013	-10.46	0.26
750	16.8	0.512062	0.000012	-11.25	0.24

Table S2: Detrital Nd and Sr isotopes from core MD77-191. E_{Nd} values were calculated using a CHUR value of 0.512638 [*Jacobsen and Wasserburg, 1980*] as follows: ε_{Nd} =$[(^{143}Nd/^{144}Nd)_{meas}/0.512638 - 1] * 10000$. Also shown are analyses of rock standard BCR-2. Uncertainties (2σ) for $^{143}Nd/^{144}Nd$ represent the standard internal error. Uncertainties (2σ) for ε_{Nd} and $^{87}Sr/^{86}Sr$ represent the external reproducibility, unless the internal error is larger.

Depth (cm)	Age (ka)	$^{143}Nd/^{144}Nd$	±2 sigma	ε_{Nd}	±2 sigma	$^{87}Sr/^{86}Sr$	±2 sigma
20	1.1	0.511753	0.000003	-17.26	0.10	0.723135	0.000009
60	2.0	0.511772	0.000009	-16.89	0.18	0.721365	0.000009
140	3.0	0.511729	0.000005	-17.73	0.10	0.721049	0.000008
210	4.1	0.511724	0.000009	-17.83	0.18	0.723225	0.000008
270	5.1	0.511733	0.000002	-17.65	0.10	0.722559	0.000010
340	6.1	0.511712	0.000006	-18.06	0.12	0.722800	0.000009
380	6.9	0.511708	0.000008	-18.14	0.16	0.720737	0.000008
410	8.1	0.511751	0.000003	-17.30	0.10	0.720911	0.000009
440	9.2	0.511797	0.000007	-16.41	0.14	0.721853	0.000008
470	10.2	0.511804	0.000004	-16.27	0.10	0.719428	0.000008
500	11.2	0.511856	0.000003	-15.25	0.10	0.721272	0.000008
530	12.2	0.511949	0.000006	-13.44	0.12	0.721316	0.000009
560	13.2	0.511909	0.000005	-14.22	0.10	0.718049	0.000009
590	14.1	0.511847	0.000002	-15.43	0.10	0.721768	0.000008
640	15.0	0.511977	0.000005	-12.89	0.10	0.718827	0.000008
700	16.0	0.511874	0.000004	-14.90	0.10	0.723879	0.000009
750	16.8	0.511868	0.000003	-15.02	0.10	0.724494	0.000008
BCR-2		0.512629	0.000009	-0.18	0.18	0.705014	0.000007
BCR-2		0.512640	0.000005	0.04	0.10	0.705026	0.000007

Table S3: Global synthesis of intermediate water circulation records spanning the deglaciation and the Holocene (see also SFig. 9). Note: ++ very strong, + strong, - weak.

Ocean basin	**No**	**Region**	**Site name**	**Latitude**	**Longitude**	**Water Depth**	**Proxy**	**Early Holocene 10-8 kyr**	**YD 13.5-11.5 kyr**	**HS1 17.5–14.7 kyr**	**References**
Atlantic Ocean	**1**	**Brazil margin**	**GeoB2107-3**	**27.2°S**	**46.5°W**	**1050 m**	**Foram ε_{Nd}**	++	–	–	[*Howe et al.*, 2016]
	2	**Brazil margin**	**KNR159-5-36GGC**	**27.5°S**	**46.5°W**	**1268 m**	**Foram ε_{Nd}**	++	–	–	[*Howe et al.*, 2016]
	3	**Portuguese margin**	**SO75-26KL**	**37.8°N**	**9.5°W**	**1099 m**	**Benthic $\delta^{13}C$**	+	++	++	[*Zahn et al.*, 1997]
	4	**Moroccan margin**	**M16004**	**30.0°N**	**10.7°W**	**1512 m**	**Benthic $\delta^{13}C$**	+	++	++	[*Zahn et al.*, 1987]
	5	**North Atlantic**	**NEAP 4K**	**61.3°N**	**24.2°W**	**1627 m**	**Benthic $\delta^{13}C$**	+	++	++	[*Rickaby and Elderfield*, 2005]
	6	**Florida Straits**	**KNR166-2-26JPC**	**24.3°N**	**83.3°W**	**546 m**	**leached εNd**	+	–	–	[*Xie et al.*, 2012]
	7	**Florida Straits**	**KNR166-2-31JPC**	**24.2°N**	**83.3°W**	**751 m**	**leached ε_{Nd}**	+	–	–	[*Xie et al.*, 2012]
	8	**Brazil margin**	**C1 (corals)**	**22.4°S**	**40.1°W**	**621 m**	**$\Delta^{14}C$**	++	++	+	[*Mangini et al.*, 2010]
	9	**Tobago Basin**	**M78/1-235-1**	**11.6°N**	**61.0°W**	**852 m**	**Benthic $\delta^{13}C$**	+	++	++	[*Poggemann et al.*, 2017]
	10	**Demerara Rise**	**KNR197-3-25GGC**	**7.7°N**	**53.8°W**	**671 m**	**Foram ε_{Nd}**	+	–	–	[*Huang et al.*, 2014]
	11	**Demerara Rise**	**KNR197-3-46CDH**	**7.8°N**	**53.7°W**	**947 m**	**Foram ε_{Nd}**	+	–	–	[*Huang et al.*, 2014]
	12	**Demerara Rise**	**KNR-197-3-9GGC**	**7.9°N**	**53.6°W**	**1100 m**	**Foram ε_{Nd}**	+	–	–	[*Huang et al.*, 2014]
	13	**Bonaire Basin**	**VM12-107**	**11.3°N**	**66.6°W**	**1079 m**	**Fish teeth/debris ε_{Nd}**	+	–	–	[*Xie et al.*, 2014]
Indian Ocean	**14**	**Tropical Indian Ocean**	**MD77-191**	**7.3°N**	**76.4°E**	**1254 m**	**Foram ε_{Nd}**	++	+	+	this study
	15	**Bay of Bengal**	**MD77-176**	**14.5°N**	**93.10°E**	**1375 m**	**$\Delta^{14}C$**	+	++	++	[*Ma et al.*, 2019]
	16	**Bay of Bengal**	**MD77-176**	**14.5°N**	**93.10°E**	**1375 m**	**Foram ε_{Nd}**	++	++	++	[*Yu et al.*, 2018]
	17	**Arabian Sea**	**RC27-14**	**18.3°N**	**57.6°E**	**596 m**	**$\Delta^{14}C$**	+	++	++	[*Bryan et al.*, 2010]
	18	**Arabian Sea**	**RC27-23**	**18°N**	**57.6°E**	**820 m**	**$\Delta^{14}C$**	+	++	++	[*Bryan et al.*, 2010]
	19	**Western Indian Ocean**	**GeoB12615-4**	**7.12°S**	**39.6°W**	**446 m**	**Benthic $\delta^{13}C$**	++	+	+	[*Romahn et al.*, 2014]

	20	**continental slope off Somalia**	**NIOP 905**	**10.7°N**	**52.0°E**	**1580 m**	**Benthic $\delta^{13}C$**	+	++	++	[Simon J. A. Jung et al., 2009]
Pacific Ocean	**21**	**Eastern Equatorial Pacific**	**TR163-19**	**2.3°N**	**91.0°W**	**2348 m**	**Planktic $\delta^{13}C$**	++	+	+	[Spero and Lea, 2002]
	22	**Southern Baja California**	**MV99-MC19/GC31/PC08**	**23.5°N**	**111.60°W**	**705 m**	**Fish teeth/debris ε_{Nd}**	+	++	++	[Basak et al., 2010]
	23	**Carnegie Ridge**	**ODP Site 1240**	**0.0°N**	**86.5°W**	**2921 m**	**Planktic $\delta^{13}C$**	+	++	++	[Pena et al., 2008]
	24	**Southern Baja California**	**MV99-MC19/GC31/PC08**	**23.5°N**	**111.60°W**	**705 m**	**$\Delta^{14}C$**	+	++	++	[Marchitto et al., 2007]
	25	**South of New Zealand**	**MD97-2120**	**45.5°S**	**174.9°E**	**1210 m**	**Benthic $\delta^{13}C$**	++	+	+	[Pahnke and Zahn, 2005]
	26	**Eastern Equatorial Pacific**	**VM21-30**	**1.2°S**	**89.7°W**	**617 m**	**$\Delta^{14}C$**	+	++	++	[Stott et al., 2009]

References

Amakawa, H., T.-L. Yu, H. Tazoe, H. Obata, T. Gamo, Y. Sano, C.-C. Shen, and K. Suzuki (2019), Neodymium concentration and isotopic composition distributions in the southwestern Indian Ocean and the Indian sector of the Southern Ocean, *Chemical Geology*, *511*, 190-203.

Basak, C., E. E. Martin, K. Horikawa, and T. M. Marchitto (2010), Southern Ocean source of ^{14}C-depleted carbon in the North Pacific Ocean during the last deglaciation, *Nature Geoscience*, *3*(11), 770-773.

Bassinot, F. C., C. Marzin, P. Braconnot, O. Marti, E. Mathienblard, F. Lombard, and L. Bopp (2011), Holocene evolution of summer winds and marine productivity in the tropical Indian Ocean in response to insolation forcing: data-model comparison, *Climate of the Past*, *7*(3), 815-829.

Battisti, D., Q. Ding, and G. Roe (2014), Coherent pan‐Asian climatic and isotopic response to orbital forcing of tropical insolation, *Journal of Geophysical Research: Atmospheres*, *119*(21), 11,997-912,020.

Blaauw, M., and J. A. Christen (2011), Flexible paleoclimate age-depth models using an autoregressive gamma process, *Bayesian analysis*, *6*(3), 457-474.

Broecker, W. S., and T. H. Peng (1982), Tracers in the Sea, *LamontDoherty Geological Observatory, Palisades, NY*.

Bryan, S. P., T. M. Marchitto, and S. J. Lehman (2010), The release of ^{14}C-depleted carbon from the deep ocean during the last deglaciation: Evidence from the Arabian Sea, *Earth and Planetary Science Letters*, *298*(1–2), 244-254.

Burton, K. W., and D. Vance (2000), Glacial–interglacial variations in the neodymium isotope composition of seawater in the Bay of Bengal recorded by planktonic foraminifera, *Earth and Planetary Science Letters*, *176*(3), 425-441.

Cheng, H., R. L. Edwards, A. Sinha, C. Spötl, L. Yi, S. Chen, M. Kelly, G. Kathayat, X. Wang, and X. Li (2016), The Asian monsoon over the past 640,000 years and ice age terminations, *nature*, *534*(7609), 640-646.

Colin, C., L. Turpin, J. Bertaux, A. Desprairies, and C. Kissel (1999), Erosional history of the Himalayan and Burman ranges during the last two glacial–interglacial cycles, *Earth and Planetary Science Letters*, *171*(4), 647-660.

Colin, C., L. Turpin, D. Blamart, N. Frank, C. Kissel, and S. Duchamp (2006), Evolution of weathering patterns in the Indo‐Burman Ranges over the last 280 kyr: Effects of sediment provenance on $^{87}Sr/^{86}Sr$ ratios tracer, *Geochemistry, Geophysics, Geosystems*, *7*(3).

Comas-Bru, L., K. Atsawawaranunt, and S. Harrison (2020), SISAL (Speleothem Isotopes Synthesis and AnaLysis Working Group) database version 2.0.

Contreras-Rosales, L. A., T. Jennerjahn, T. Tharammal, V. Meyer, A. Lückge, A. Paul, and E. Schefuß (2014), Evolution of the Indian Summer Monsoon and terrestrial vegetation in the Bengal region during the past 18ka, *Quaternary Science Reviews*, *102*(102), 133-148.

Du, J., B. A. Haley, and A. C. Mix (2020), Evolution of the Global Overturning Circulation since the Last Glacial Maximum based on marine authigenic neodymium isotopes, *Quaternary Science Reviews*, *241*, 106396.

Goswami, V., S. K. Singh, and R. Bhushan (2014), Impact of water mass mixing and dust deposition on Nd concentration and ε_{Nd} of the Arabian Sea water column, *Geochimica et*

Cosmochimica Acta, *145*, 30-49.

Grootes, P. M., and M. Stuiver (1997), Oxygen 18/16 variability in Greenland snow and ice with 10^3- to 10^5-year time resolution, *Journal of Geophysical Research Oceans*, *102*(C12), 26455-26470.

Heaton, T. J., P. Köhler, M. Butzin, E. Bard, R. W. Reimer, W. E. Austin, C. B. Ramsey, P. M. Grootes, K. A. Hughen, and B. Kromer (2020), Marine20—the marine radiocarbon age calibration curve (0–55,000 cal BP), *Radiocarbon*, *62*(4), 779-820.

Howe, J. N., A. M. Piotrowski, D. W. Oppo, K. F. Huang, S. Mulitza, C. M. Chiessi, and J. Blusztajn (2016), Antarctic intermediate water circulation in the South Atlantic over the past 25,000 years, *Paleoceanography*, *31*.

Hu, R., T. L. Noble, A. M. Piotrowski, I. N. Mccave, H. C. Bostock, and H. L. Neil (2016), Neodymium isotopic evidence for linked changes in Southeast Atlantic and Southwest Pacific circulation over the last 200 kyr, *Earth and Planetary Science Letters*, *455*, 106-114.

Huang, K.-F., D. W. Oppo, and W. B. Curry (2014), Decreased influence of Antarctic intermediate water in the tropical Atlantic during North Atlantic cold events, *Earth and Planetary Science Letters*, *389*, 200-208.

Jacobsen, S. B., and G. Wasserburg (1980), Sm-Nd isotopic evolution of chondrites, *Earth and Planetary Science Letters*, *50*(1), 139-155.

Jung, S. J. A., G. M. Ganssen, and G. R. Davies (2001), Multidecadal variations in the Early Holocene outflow of Red Sea water into the Arabian Sea, *Paleoceanography*, *16*(6), 658-668.

Jung, S. J. A., D. Kroon, G. Ganssen, F. Peeters, and R. Ganeshram (2009), Enhanced Arabian Sea intermediate water flow during glacial North Atlantic cold phases, *Earth & Planetary Science Letters*, *280*(1–4), 220-228.

Kaushal, N., S. F. Breitenbach, F. A. Lechleitner, A. Sinha, V. C. Tewari, S. M. Ahmad, M. Berkelhammer, S. Band, M. Yadava, and R. Ramesh (2018), The Indian summer monsoon from a speleothem $\delta^{18}O$ perspective—a review, *Quaternary*, *1*(3), 29.

Kraft, S., M. Frank, E. C. Hathorne, and S. Weldeab (2013), Assessment of seawater Nd isotope signatures extracted from foraminiferal shells and authigenic phases of Gulf of Guinea sediments, *Geochimica et Cosmochimica Acta*, *121*, 414-435.

Kudrass, H. R., A. Hofmann, H. Doose, K. Emeis, and H. Erlenkeuser (2001), Modulation and amplification of climatic changes in the Northern Hemisphere by the Indian summer monsoon during the past 80 k.y, *Geology*, *29*(1), 63-66.

Laskar, J., P. Robutel, F. Joutel, M. Gastineau, A. Correia, and B. Levrard (2004), A long-term numerical solution for the insolation quantities of the Earth, *Astronomy & Astrophysics*, *428*(1), 261-285.

Liu, W. G., S. Wei, J. Zhang, C. Ao, F. T. Liu, B. Cai, H. Y. Zhou, J. L. Yang, and C. F. Li (2020), An improved separation scheme for Sr through fluoride coprecipitation combined with a cation-exchange resin from geological samples with high Rb/Sr ratios for high-precision determination of Sr isotope ratios, *Journal of Analytical Atomic Spectrometry*, *35*.

Liu, X., J. Liu, S. Chen, J. Chen, X. Zhang, J. Yan, and F. Chen (2020), New insights on Chinese cave δ18O records and their paleoclimatic significance, *Earth-Science Reviews*, *207*, 103216.

Lugmair, G., and R. Carlson (1978), The Sm-Nd history of KREEP, paper presented at

Lunar and Planetary Science Conference Proceedings.

Ma, R., S. Sépulcre, F. Bassinot, F. Haurine, N. Tisnérat - Laborde, and C. Colin (2020), North Indian Ocean Circulation Since the Last Deglaciation as Inferred From New Elemental Ratio Records for Benthic Foraminifera Hoeglundina elegans, *Paleoceanography and Paleoclimatology*, *35*(6).

Ma, R., S. Sépulcre, L. Licari, F. Bassinot, Z. Liu, N. Tisnérat-Laborde, N. Kallel, Z. Yu, and C. Colin (2019), Changes in Intermediate Circulation in the Bay of Bengal Since the Last Glacial Maximum as Inferred From Benthic Foraminifera Assemblages and Geochemical Proxies, *Geochemistry, Geophysics, Geosystems*, *20*(3), 1592-1608.

Mangini, A., J. M. Godoy, M. L. Godoy, R. Kowsmann, G. M. Santos, M. Ruckelshausen, A. Schroeder-Ritzrau, and L. Wacker (2010), Deep sea corals off Brazil verify a poorly ventilated Southern Pacific Ocean during H2, H1 and the Younger Dryas, *Earth and Planetary Science Letters*, *293*(3-4), 269-276.

Marchitto, T. M., S. J. Lehman, J. D. Ortiz, J. Flückiger, and G. A. Van (2007), Marine radiocarbon evidence for the mechanism of deglacial atmospheric CO_2 rise, *Science*, *316*(5830), 1456.

Pahnke, K., and R. Zahn (2005), Southern Hemisphere Water Mass Conversion Linked with North Atlantic Climate Variability, *Science*, *307*(5716), 1741-1746.

Palmer, M. (1985), Rare earth elements in foraminifera tests, *Earth and planetary science letters*, *73*(2-4), 285-298.

Pena, L. D., I. Cacho, P. Ferretti, and M. A. Hall (2008), El Niño - Southern Oscillation–like variability during glacial terminations and interlatitudinal teleconnections, *Paleoceanography*, *23*(3).

Pena, L. D., S. L. Goldstein, S. R. Hemming, K. M. Jones, E. Calvo, C. Pelejero, and I. Cacho (2013), Rapid changes in meridional advection of Southern Ocean intermediate waters to the tropical Pacific during the last 30kyr, *Earth and Planetary Science Letters*, *368*, 20-32.

Piotrowski, A., A. Galy, J. Nicholl, N. Roberts, D. Wilson, J. Clegg, and J. Yu (2012), Reconstructing deglacial North and South Atlantic deep water sourcing using foraminiferal Nd isotopes, *Earth and Planetary Science Letters*, *357*, 289-297.

Poggemann, D.-W., E. C. Hathorne, D. Nürnberg, M. Frank, I. Bruhn, S. Reißig, and A. Bahr (2017), Rapid deglacial injection of nutrients into the tropical Atlantic via Antarctic Intermediate Water, *Earth and Planetary Science Letters*, *463*, 118-126.

Prasad, T. G., M. Ikeda, and S. P. Kumar (2001), Seasonal spreading of the Persian Gulf Water mass in the Arabian Sea, *Journal of Geophysical Research: Oceans*, *106*(C8), 17059.

Rickaby, R. E. M., and H. Elderfield (2005), Evidence from the high-latitude North Atlantic for variations in Antarctic Intermediate water flow during the last deglaciation, *Geochemistry, Geophysics, Geosystems*, *6*(5).

Roberts, N., A. Piotrowski, H. Elderfield, T. Eglinton, and M. Lomas (2012), Rare earth element association with foraminifera, *Geochimica et Cosmochimica Acta*, *94*, 57-71.

Roberts, N. L., A. M. Piotrowski, J. F. McManus, and L. D. Keigwin (2010), Synchronous Deglacial Overturning and Water Mass Source Changes, *Science*, *327*(5961), 75-78.

Robinson, L. F., and T. van de Flierdt (2009), Southern Ocean evidence for reduced export of North Atlantic Deep Water during Heinrich event 1, *Geology*, *37*(3), 195.

Rohling, E. J., and W. J. Zachariasse (1996), Red Sea outflow during the last glacial maximum, *Quaternary International*, *31*, 77-83.

Romahn, S., A. Mackensen, J. Groeneveld, and J. Pätzold (2014), Deglacial intermediate water reorganization: new evidence from the Indian Ocean, *Clim. Past*, *10*(1), 293-303.

Singh, S. P., S. K. Singh, V. Goswami, R. Bhushan, and V. K. Rai (2012), Spatial distribution of dissolved neodymium and εNd in the Bay of Bengal: role of particulate matter and mixing of water masses, *Geochimica et Cosmochimica Acta*, *94*, 38-56.

Spero, H. J., and D. W. Lea (2002), The Cause of Carbon Isotope Minimum Events on Glacial Terminations, *Science*, *296*(5567), 522-525.

Stoll, H. M., D. Vance, and A. Arevalos (2007), Records of the Nd isotope composition of seawater from the Bay of Bengal: Implications for the impact of Northern Hemisphere cooling on ITCZ movement, *Earth and Planetary Science Letters*, *255*(1), 213-228.

Stott, L., J. Southon, A. Timmermann, and A. Koutavas (2009), Radiocarbon age anomaly at intermediate water depth in the Pacific Ocean during the last deglaciation, *Paleoceanography*, *24*(2), -.

Tachikawa, K., A. M. Piotrowski, and G. Bayon (2014), Neodymium associated with foraminiferal carbonate as a recorder of seawater isotopic signatures, *Quaternary Science Reviews*, *88*, 1-13.

Tachikawa, K., T. Toyofuku, I. Basile-Doelsch, and T. Delhaye (2013), Microscale neodymium distribution in sedimentary planktonic foraminiferal tests and associated mineral phases, *Geochimica et Cosmochimica Acta*, *100*, 11-23.

Tanaka, T., et al. (2000), JNdi-1: a neodymium isotopic reference in consistency with LaJolla neodymium, *Chemical Geology*, *168*(3), 279-281.

Weis, D., et al. (2006), High-precision isotopic characterization of USGS reference materials by TIMS and MC-ICP-MS, *Geochemistry, Geophysics, Geosystems*, *7*(8).

Wilson, D. J., A. M. Piotrowski, A. Galy, and V. K. Banakar (2015), Interhemispheric controls on deep ocean circulation and carbon chemistry during the last two glacial cycles, *Paleoceanography*, *30*(6), 621-641.

Wu, Q., C. Colin, Z. Liu, F. Thil, Q. Dubois - Dauphin, N. Frank, K. Tachikawa, L. Bordier, and E. Douville (2015), Neodymium isotopic composition in foraminifera and authigenic phases of the South China Sea sediments: Implications for the hydrology of the North Pacific Ocean over the past 25 kyr, *Geochemistry, Geophysics, Geosystems*, *16*(11), 3883-3904.

Xie, R. C., F. Marcantonio, and M. W. Schmidt (2012), Deglacial variability of Antarctic Intermediate Water penetration into the North Atlantic from authigenic neodymium isotope ratios, *Paleoceanography*, *27*(3).

Xie, R. C., F. Marcantonio, and M. W. Schmidt (2014), Reconstruction of intermediate water circulation in the tropical North Atlantic during the past 22,000years, *Geochimica et Cosmochimica Acta*, *140*, 455-467.

Yu, Z., C. Colin, F. Bassinot, S. Wan, and G. Bayon (2020), Climate-Driven Weathering Shifts Between Highlands and Floodplains, *Geochemistry, Geophysics, Geosystems*, *21*(7), e2020GC008936.

Yu, Z., C. Colin, L. Meynadier, E. Douville, A. Dapoigny, G. Reverdin, Q. Wu, S. Wan, L. Song, and Z. Xu (2017), Seasonal variations in dissolved neodymium isotope composition in the Bay of Bengal, *Earth and Planetary Science Letters*, *479*, 310-321.

Yu, Z., C. Colin, R. Ma, L. Meynadier, S. Wan, Q. Wu, N. Kallel, S. Sepulcre, A.

Dapoigny, and F. Bassinot (2018), Antarctic Intermediate Water penetration into the Northern Indian Ocean during the last deglaciation, *Earth and Planetary Science Letters*, *500*, 67-75.

Yu, Z., et al. (2019), Sea level-controlled sediment transport to the eastern Arabian Sea over the past 600 kyr: Clay minerals and SrNd isotopic evidence from IODP site U1457, *Quaternary Science Reviews*, *205*, 22-34.

Zahn, R., M. Sarnthein, and H. Erlenkeuser (1987), Benthic isotope evidence for changes of the Mediterranean outflow during the Late Quaternary, *Paleoceanography*, *2*(6), 543-559.

Zahn, R., J. Schnfeld, H. R. Kudrass, M. H. Park, H. Erlenkeuser, and P. Grootes (1997), Thermohaline instability in the North Atlantic during meltwater events: Stable isotope and ice‐rafted detritus records from Core SO75‐26KL, Portuguese Margin, *Paleoceanography*, *12*.

Zhao, N., D. W. Oppo, K. F. Huang, J. N. W. Howe, and L. D. Keigwin (2019), Glacial–interglacial Nd isotope variability of North Atlantic Deep Water modulated by North American ice sheet, *Nature Communications*, *10*(1), 5773.